Chemical Science

ROYAL SOCIETY OF CHEMISTRY

EDGE ARTICLE

View Article Online
View Journal | View Issue

Cite this: *Chem. Sci.*, 2025, **16**, 22542

All publication charges for this article have been paid for by the Royal Society of Chemistry

Graphene-supported covalent organic framework nanosheets for high performance aqueous dual-ion batteries

Xiya Yang,[a] Mengying Huang,[b] Guang Lu,[c] Rong Jiang,[d] Xinxin Wang,[a] Zhixin Liu,[b] Lijuan Jiao,[a] Erhong Hao,[a] Dongdong Qi,[b] Kang Wang,*[b] Qian Chen *[e] and Jianzhuang Jiang *[bf]

In situ growth of covalent organic framework (COF) nanosheets on substrates like graphene and carbon nanotubes usually leads to significantly enhanced conductivity but is often accompanied by an obvious reduction in crystallinity, thus resulting in non-ideal electrochemical performance. Herein, the hydrothermal condensation of two molecules with aromatic conjugated structures, triphenylene-2,3,6,7,10,11-hexacarboxylic acid (HATNCA) and 1,3,5-tris(4-aminophenyl) triazine (TAPT), on graphene affords a series of graphene-supported 2D COF nanosheets, HT-COF-XGs (X = 10, 20, and 30 wt% of graphene), with controllable thicknesses of 30, 11, and 7 layers. Powder X-ray diffraction (PXRD) analysis reveals the excellent crystalline nature of the nanosheets and further characterization shows that this COF has good conductivity and a large pore size of 2.0 nm, which enable fast and stable electron/ion transport. These properties, in combination with the fully exposed abundant active sites for storing Zn^{2+} ions and anchoring polyiodides, endow these graphene-supported COF nanosheets, in particular HT-COF-20%G, with the best aqueous dual-ion battery (ADIBs) performance to date with a high reversible capacity of 792 mAh g^{-1} at 2 A g^{-1} and good cycling stability of 83% capacity retention at 20 A g^{-1} after 8000 cycles.

Received 3rd July 2025
Accepted 14th October 2025

DOI: 10.1039/d5sc04918k

rsc.li/chemical-science

Introduction

The increasing demand for renewable energy has intensified the focus on developing eco-friendly and highly efficient energy storage systems.[1–4] Of late, aqueous dual-ion batteries (ADIBs) have started to attract increasing attention as a promising energy storage system for grid-scale applications owing to their remarkable energy density, inherent safety, cost-effectiveness, and environmental sustainability.[5–9] Among the charge carriers for ADIBs, zinc cations and iodine anions are particularly noteworthy due to their abundance, high capacity, and suitable redox potentials.[10–12] In contrast to conventional zinc ion batteries, ADIBs operate through the migration of cations and anions during the charging/discharging processes, not only circumventing the drawbacks associated with Zn^{2+} intercalation but also accelerating the Zn plating/stripping reaction.[13,14] Unfortunately, the notorious shuttle effect and slow ion transport kinetics of the iodine species have significantly hindered the development of ADIBs for use in practical grid storage applications.[15,16] Despite the great application potential of ADIBs, thus far only a few types of porous materials including carbon materials,[17–19] organic polymers,[20,21] and metal–organic frameworks (MOFs)[22] have been employed as the cathode materials for ADIBs. Due to their low density, robust stability, and ordered porous structure, COFs constructed from molecular building blocks that depend on covalent bonds, as seen in their MOF counterparts but with enhanced stability, are expected to show promise in ADIBs.[23–27] However, COF-based ADIBs still remain essentially unexplored with the sole example being, to the best of our knowledge, IISERP-COF22.[28]

It is worth noting that bulky 2D COFs with densely packed layers have a substantial number of buried active sites and

[a]*Key Laboratory of Functional Molecular Solids, Ministry of Education, College of Chemistry and Materials Science, Anhui Normal University, Wuhu, Anhui, 241002, China*

[b]*Beijing Key Laboratory for Science and Application of Functional Molecular and Crystalline Materials, Department of Chemistry and Chemical Engineering, School of Chemistry and Biological Engineering, University of Science and Technology Beijing, Beijing 100083, China. E-mail: kangwang@ustb.edu.cn; jianzhuang@ustb.edu.cn*

[c]*College of Chemical and Biological Engineering, Shandong University of Science and Technology, Qingdao 266590, China*

[d]*State Key Laboratory of Chemical Resource Engineering, Beijing Engineering Center for Hierarchical Catalysts, College of Chemistry, Beijing University of Chemical Technology, Beijing 100029, China*

[e]*Institute of Functional Nano & Soft Materials (FUNSOM), Jiangsu Key Laboratory for Carbon-Based Functional Materials & Devices, Soochow University, Suzhou 215123, China. E-mail: chenqian@suda.edu.cn*

[f]*Key Laboratory of Macrocyclic and Supramolecular Chemistry of Guizhou Province, School of Chemistry and Chemical Engineering, Guizhou University, Guiyang 550025, China*

restrict ionic transport to quite a large extent,[29] thus leading to unsatisfactory power and energy densities. Fortunately, bulky 2D COFs can be exfoliated into nanosheets, enabling the exposure of more accessible active sites and the enhancement of ion diffusion.[30–33] For the purpose of enhancing the conductivity, graphene and carbon nanotubes were employed for the fabrication of substrate-supported thin COFs nanosheets.[34,35] However, the incorporation of substrates into COFs usually leads to a significant reduction in the crystallinity due to the disruption that the corresponding substrate has on the molecular arrangement of the building blocks, interfering with the crystal growth and repair process.[36–39] This in turn compromises the inherent advantages of the ordered COFs structure to a certain extent. As a result, achieving substrate-supported thin COFs nanosheets with high crystallinity remains a challenge.

Herein, two highly conjugated organic precursors were selected to pre-organize a molecular assembly through π–π stacking interactions with graphene. This strategy enables the controlled directional growth of COFs along the graphene substrate, significantly mitigating the adverse effects on the crystallinity of the COFs. Specifically, a series of graphene-supported COF nanosheets HT-COF-XGs (X = 10, 20, and 30 wt% of graphene) with controllable thicknesses of 30, 11, and 7 layers were prepared *via in situ* hydrothermal condensation of triphenylene-2,3,6,7,10,11-hexacarboxylic acid (HATNCA) and 1,3,5-tris(4-aminophenyl) triazine (TAPT) on graphene. The aromatic conjugated structure of HATNCA and TAPT facilitates their effective π–π interaction with graphene, resulting in the isolation of HT-COF-XGs with high crystallinity and a well-defined hexagonal porous structure, as demonstrated using powder X-ray diffraction (PXRD) analysis and high-resolution transmission electron microscopy (HR-TEM), respectively. HT-COF-XGs possesses excellent stability, good conductivity, and a large pore size of 2.0 nm, enabling fast and stable electron/ion transport. These properties, in combination with the abundant fully exposed active sites for storing Zn^{2+} ions and anchoring active polyiodides, endow HT-COF-XGs, in particular HT-COF-20%G, with excellent ADIBs performance with a high reversible capacity of 792 mAh g^{-1} at 2 A g^{-1}, remarkable rate performance (a capacity of 520 mAh g^{-1}, an energy density of 461 W h kg^{-1}, and a power density of 22 734 W kg^{-1} at 20 A g^{-1}), and good cycling stability (83% capacity retention at 20 A g^{-1} after 8000 cycles), surpassing all the thus far reported ADIBs electrodes.

Results and discussion

Synthesis and characterization

In this work, pristine HT-COF was isolated in a yield of 92% from the condensation of HATNCA and TAPT in pure water at 200 °C for 48 hours. The HT-COF-XGs nanosheets including HT-COF-10%G, HT-COF-20%G, and HT-COF-30%G were fabricated in the same manner by adding 10, 20, and 30 wt% of graphene, respectively, resulting in yields of 92–95% (Fig. S1 and Scheme 1). The HT-COF structure was first characterized using Fourier-transform infrared (FT-IR) spectroscopy *via* observation of the characteristic stretching vibration bands of C=O and C–N–C at 1781–1725 and 1357 cm^{-1}, respectively.

The disappearance of the TAPT amino band at 3300 cm^{-1} and a reduced intensity for the HATNCA carboxyl groups at 1716 cm^{-1} demonstrate the successful polymerization of the starting reagents and the formation of imide groups[40] (Fig. 1a). In the solid-state ^{13}C cross-polarization magic angle spinning nuclear magnetic resonance spectrum of HT-COF, the carbonyl carbon of the imide moiety appears at 164 ppm, while the aryl carbon atoms in the triazine and benzene moieties appear at 167 and 110–155 ppm,[41] respectively, providing additional evidence for the formation of imide groups (Fig. 1b). The FT-IR spectra of HT-COF-XGs also display corresponding characteristic evidence for the formation of imide groups through the bands at 1781–1725 and 1357 cm^{-1}, thus evidencing the presence of HT-COF on graphene (Fig. S2).

HT-COF was structurally characterized through PXRD analysis in combination with theoretical simulation. In the PXRD pattern in Fig. 1c, HT-COF displays an intense peak at $2\theta \approx 3.87°$ together with four prominent peaks at 6.69°, 7.78°, 10.23°, and 25.95° due to the (1,0,0), (2,−1,0), (2,0,0), (3,−1,0), and (0,0,1) planes, respectively, thus proving its highly crystalline nature. Density-functional tight-binding ($DFTB^+$) calculations were performed to afford the optimum C_3 + C_3 hexagonal skeleton and stacking mode of HT-COF. As can be seen in Fig. 1c and S3, the simulated AA stacking model can generate a PXRD profile that reproduces the experimental pattern well with good agreement factors of R_p = 4.01% and R_{wp} = 5.70% according to the Le Bail refinement. The cell parameters were determined to be $\alpha = \beta = 90°$, $\gamma = 120°$, $a = b = 25.93$ Å, $c = 3.38$ Å in the $P\bar{6}m2$ group space. According to the structural model of HT-COF, the theoretical size of the circular hole is 2.0 nm and the π–π stacking distance is 0.34 nm (Fig. 1d and e). Interestingly, unlike other COFs/graphene composites reported previously,[36,42–45] the isolated HT-COF-XGs still display clear diffraction peaks due to the (1,0,0), (2,−1,0), (2,0,0), (3,−1,0), and (0,0,1) planes, the same as those in the pristine HT-COF (Fig. 1f) revealing that the excellent crystallinity of the HT-COF nanosheets is maintained on the graphene substrate. This suggests that a graphene template effect exists that facilitates the formation of COFs with good crystallinity due to the effective π–π interactions with the aromatic conjugated structures of the precursors.

The porosities of HT-COF and HT-COF-XGs were assessed by N_2 sorption measurements at 77 K. As shown in Fig. 1g, HT-COF and HT-COF-XGs display type IV isotherms with the presence of a hysteresis loop, indicating the mesoporous nature of their structures. The Brunauer–Emmett–Teller (BET) surface area of the HT-COF amounts to 1219 m^2 g^{-1}. According to the pore size distribution, the HT-COF possesses a distinct type of mesopore with a width of 2.0 nm (Fig. S4) consistent with the theoretically calculated value of 2.0 nm based on the AA stacking structural model mentioned above. The introduction of graphene leads to reduced isotherms under low pressure and BET surface areas of 1080, 1023, and 826 m^2 g^{-1} for HT-COF-10%G, HT-COF-20%G, and HT-COF-30%G, respectively. Additionally, thermogravimetric analysis (TGA) reveals that HT-COF and HT-COF-XGs

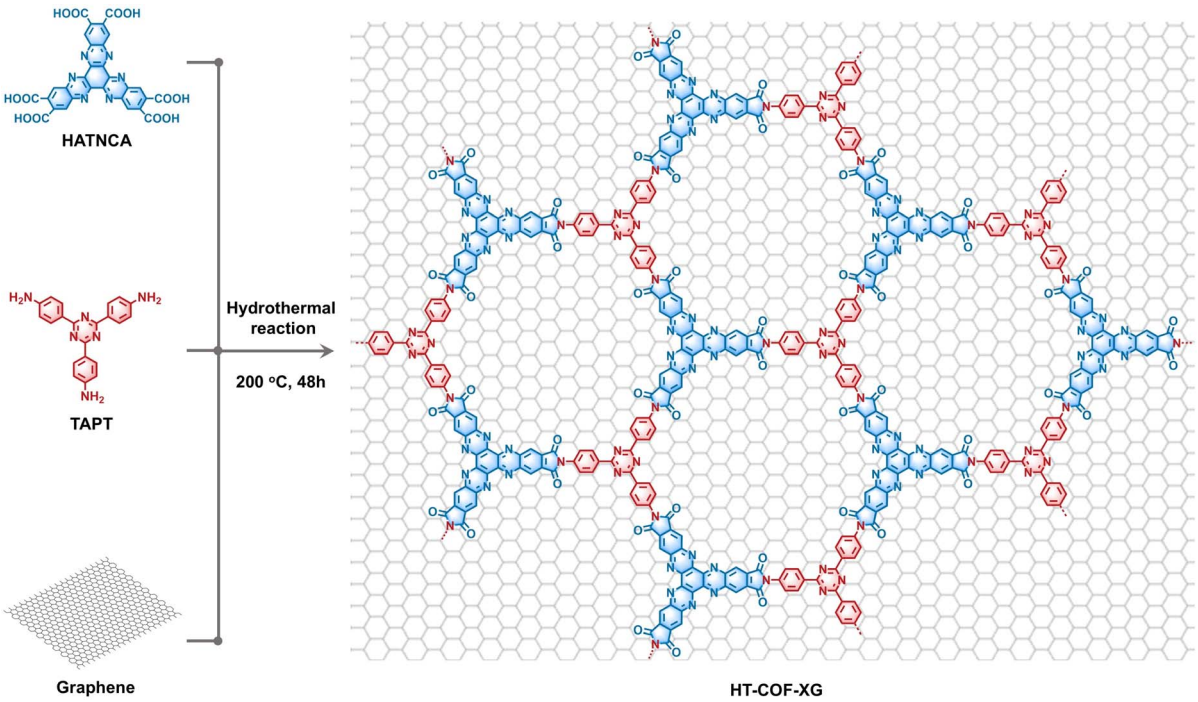

Scheme 1 Schematic representation of the synthesis of HT-COF-XGs.

have good thermal stability with a decomposition temperature above 400 °C in an N_2 atmosphere (Fig. S5). Next, HT-COF-20%G was employed as a typical representative to investigate the chemical stability of this series of materials. As displayed in Fig. S6, after being soaked in a series of solvents including tetrahydrofuran (THF), methanol (MeOH), *N*-methyl-2-pyrrolidone (NMP), *N*,*N*-dimethylformamide (DMF), and 6 M hydrochloric acid (HCl) for seven days, the PXRD patterns of HT-COF-20%G remained almost unchanged, revealing its excellent solvent resistance. This is also true for this material in a 3.0 M $ZnSO_4$ + 0.5 M KI electrolyte in water, thus showing that HT-COF-XGs have favorable electrode stability for ADIBs application.

The pristine HT-COF shows a fibrous morphology with diameters ranging from 50 to 200 nm based on the scanning electron microscopy (SEM) and transmission electron microscopy (TEM) images in Fig. S7 and S8. HR-TEM images confirm the presence of a well-ordered network with a lattice spacing of 2.27 nm corresponding to the (1,0,0) plane (Fig. S8). The use of graphene during the COF synthesis process results in preferential growth along its surface because of the π–π interactions between the precursors and graphene, resulting in the formation of COF/graphene nanosheets. As a result, the morphology of HT-COF evolves from fibrous blocks into nanosheets that are tightly anchored onto graphene, leading to the composite nanosheets seen in the SEM images in Fig. S9. As revealed by the TEM images in Fig. 2a–c, S10 and S11, HT-COF-XGs demonstrates significantly increased surface roughness compared to the smooth surface of pristine graphene due to the uniform deposition of HT-COF onto the graphene substrate. The element energy dispersive spectroscopy (EDS) mapping images reveal a homogeneous distribution of C, O, and N over HT-COF-20%G (Fig. S12) further confirming the uniform distribution of HT-COF on graphene. Additionally, the well-organized structure of HT-COF on the graphene substrate in the HT-COF-20%G nanosheets allows the visualization of its hexagonal porous architecture through HR-TEM analysis (Fig. 2c) further proving the excellent crystallinity of the nanosheets. For the purpose of determining the thickness of the HT-COF on the graphene substrate in the HT-COF-XGs nanosheets, these composites and graphene were comparatively investigated using atomic force microscopy (AFM). As shown in Fig. 2d and e, the thickness of graphene is approximately 1.3 nm, corresponding to a three-layer structure, while the average thicknesses of HT-COF-10%G, HT-COF-20%G, and HT-COF-30%G, amount to 11.8, 5.0, and 3.6 nm, respectively, corresponding to approximately 30, 11, and 7 layers of HT-COF, respectively (Fig. 2f, g and S13).

Electrochemical performance

Inspired by their dense redox-active sites and excellent conductivity, as detailed below, together with the presence of well-ordered porous nanosheets that can shorten the ion diffusion length and improve active site accessibility, the HT-COF-XGs nanosheets were employed in the fabrication of an ADIBs cathode. The redox mechanism of the HT-COF-XGs in the ADIBs was investigated using cyclic voltammetry (CV). Taking HT-COF-20%G as a typical representative, the impact of the electrolyte composition on the redox behavior within a voltage range of 0.2 to 1.5 V was initially investigated. When 3 M $ZnSO_4$ is used as the electrolyte, the HT-COF-20%G cathode shows two pairs of weak redox peaks at 1.02/0.78 V and 0.77/0.51 V *versus* Zn/Zn^{2+}, respectively (Fig. 3a), which are assigned to the

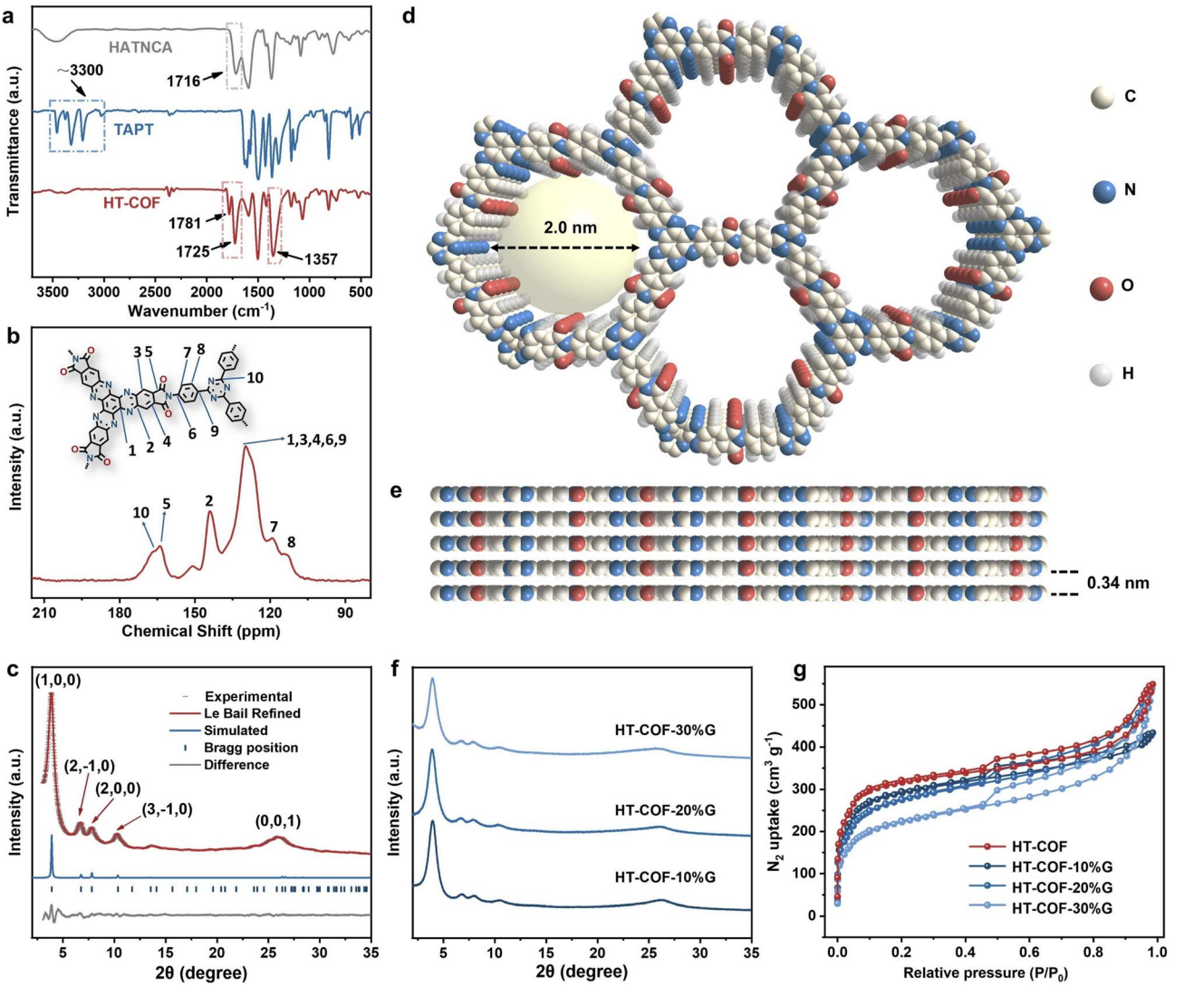

Fig. 1 Structural characterization of HT-COF and HT-COF-XGs. (a) FT-IR spectra of HT-COF, HATNCA and TAPT. (b) Solid state ^{13}C CP/MAS NMR spectrum of HT-COF. (c–e) PXRD pattern, and top/side views of the simulated AA stacking structure of HT-COF. (f) PXRD patterns of HT-COF-10%G, HT-COF-20%G, and HT-COF-30%G. (g) N_2 sorption isotherm profiles of HT-COF, HT-COF-10%G, HT-COF-20%G, and HT-COF-30%G.

reversible C=N and C=O active sites.[46,47] On the other hand, in the 0.5 M KI electrolyte, the CV curve shows a reduction peak at 1.26 V and an oxidation peak at 1.32 V with weak intensity, indicating that upon introduction of I^- into the electrolyte during the charge process I_n^- is generated and a reversible I_n^-/I^- redox process for electrochemical energy storage is formed.[20] Surprisingly, the CV curves of the HT-COF-20%G cathode exhibit a larger enclosed area with three clear redox peaks at 1.33/1.21, 0.98/0.93, and 0.65/0.51 V *versus* Zn/Zn^{2+} in 3 M $ZnSO_4$ + 0.5 M KI electrolyte corresponding to the I_n^-/I^-, C=N/C–N, and C=O/C–O redox reactions, respectively. The redox peaks for the HT-COF-20%G cathode of C=N/C–N and C=O/C–O in 3 M $ZnSO_4$ + 0.5 M KI display reduced gaps (0.14 and 0.05 V) in comparison with those in 3 M $ZnSO_4$ (0.26 and 0.24 V), indicating a decrease in polarization due to the introduction of KI, which might enhance the ion transport rate. The electrochemical process of I_n^-/I^- shows an enlarged gap between the oxidation and reduction peaks, increasing from 0.06 V to 0.11 V in the 0.5 M KI and 3 M ZnSO4 + 0.5 M KI electrolyte systems. This phenomenon can be attributed to the provision of charge balanced carriers by Zn^{2+}, which promotes more efficient iodine ion conversion and thus enhances the polarization process. Therefore, the two energy storage mechanisms (Zn^{2+} and I_n^- storage) exhibit a synergistic relationship, thereby enhancing their overall effectiveness. Furthermore, the CV curves of the HT-COF-20%G electrode display excellent overlap after the initial irreversibility, indicating the remarkable reversibility of its ion storage behavior (Fig. S14).

To investigate the rate performance, HT-COF-XGs, galvanostatic charge/discharge (GCD) tests were conducted at various current densities. All the specific capacities were determined according to the mass of the COF/graphene composites. HT-

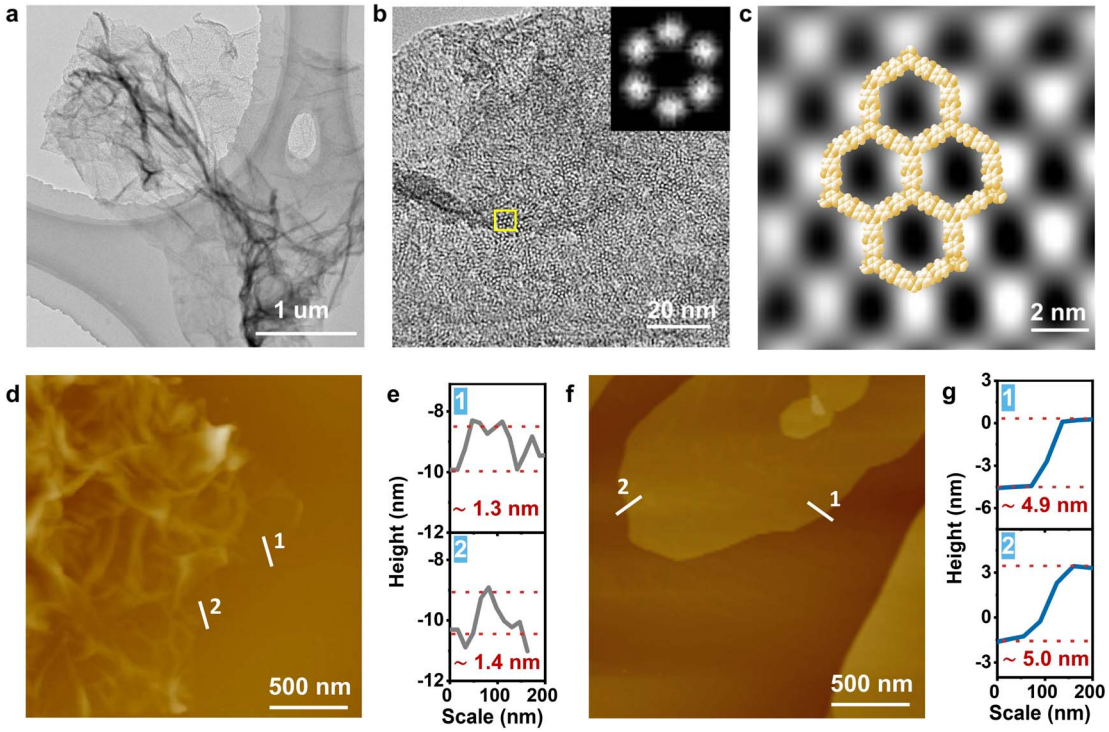

Fig. 2 Characterization of the morphology of HT-COF-20%G. (a–c) TEM and HR-TEM images of HT-COF-20%G (HT-COF on a graphene substrate). (d and e) AFM topography images and AFM height profiles of graphene. (f and g) AFM topography images and AFM height profiles of HT-COF-20%G.

COF-20%G delivers a poor specific capacity of 150 mAh g^{-1} at 2 A g^{-1}, when using 3 M $ZnSO_4$ as the electrolyte (Fig. S15 and S16), which is obviously lower than the theoretical storage capacity for Zn^{2+} storage of 216 mAh g^{-1}. When KI is added to the electrolyte the capacity is significantly enhanced, thus verifying the crucial role of iodine as an active substance in improving the electrochemical performance. During the charging process, iodine ions are oxidized into polyiodides, while HT-COF serves as a host material for anchoring polyiodides. Electrolytes containing varying concentrations of KI have also been investigated. As shown in Fig. S17, the specific capacity is also obviously increased as the concentration of KI increases. However, an excessive amount of KI may reduce the coulombic efficiency of the ADIBs because the limited number of adsorption sites in HT-COF-XGs is insufficient to effectively anchor the excess polyiodides.[20,22] As a consequence, the 3 M ZnSO4 + 0.5 M KI electrolyte was selected for subsequent electrochemical performance tests. The capacity contribution of the HT-COF-XGs in this work actually stems from two aspects: firstly, the intrinsic oxidation-active sites within HT-COF directly enhance the capacity (as observed in the range of 0.2–1.1 V in the CV curves) and secondly, the oxidation activity of iodide species provides additional improvement (as observed in the range of 1.1–1.5 V in the CV curves). As depicted in Fig. 3b, the electrochemical performance of all the HT-COF-XGs nanosheets surpasses that of HT-COF due to the enhanced exposure of active sites and increased conductivity of the former materials. Among the HT-COF-XGs nanosheets investigated, HT-COF-20%G exhibits superior capacities throughout the cycles tested. More precisely, the specific capacity of the activated HT-COF-20%G electrode is as high as 792 mAh g^{-1} after 260 cycles (the utilization rate of iodine is approximately 44%, Fig. S16) which is obviously higher than HT-COF (652 mAh g^{-1}), HT-COF-10%G (676 mAh g^{-1}), and HT-COF-30%G (660 mAh g^{-1}) at a current density of 2 A g^{-1}. In comparison with HT-COF, the enhanced specific capacity of the HT-COF-20%G electrode can be attributed to the π–π interactions between the HT-COF layers and graphene, which effectively reduce the interface resistance, shorten the ion transport pathways, and enhance the active site utilization. This is also true for the HT-COF-10%G electrode. However, the addition of greater amounts of graphene indeed leads to a reduction in nanosheet thickness but also a concomitant decrease in the COF content within the HT-COF-30%G nanosheets. This in turn diminishes the overall number of active sites and weakens the electrochemical performance. Along with increasing the current density, the HT-COF-20%G electrode delivers discharge specific capacities of 711, 640, 583, 547, 500, and 469 mAh g^{-1} at current densities of 4, 6, 8, 10, 15, and 20 A g^{-1} (Fig. 3c). As a comparison, the discharge specific capacities at the same current densities were 547, 458, 387, 348, 297, and 261 mAh g^{-1} for HT-COF, 591, 517, 446, 398, 346, and 321 mAh g^{-1} for HT-COF-10%G, and 587, 525, 473, 438, 395, and 374 mAh g^{-1} for HT-COF-30%G (Fig. 3d and S18). It is worth noting that despite the relatively low specific capacity of HT-COF-30%G due to the limited number of active sites, it demonstrates significantly superior rate

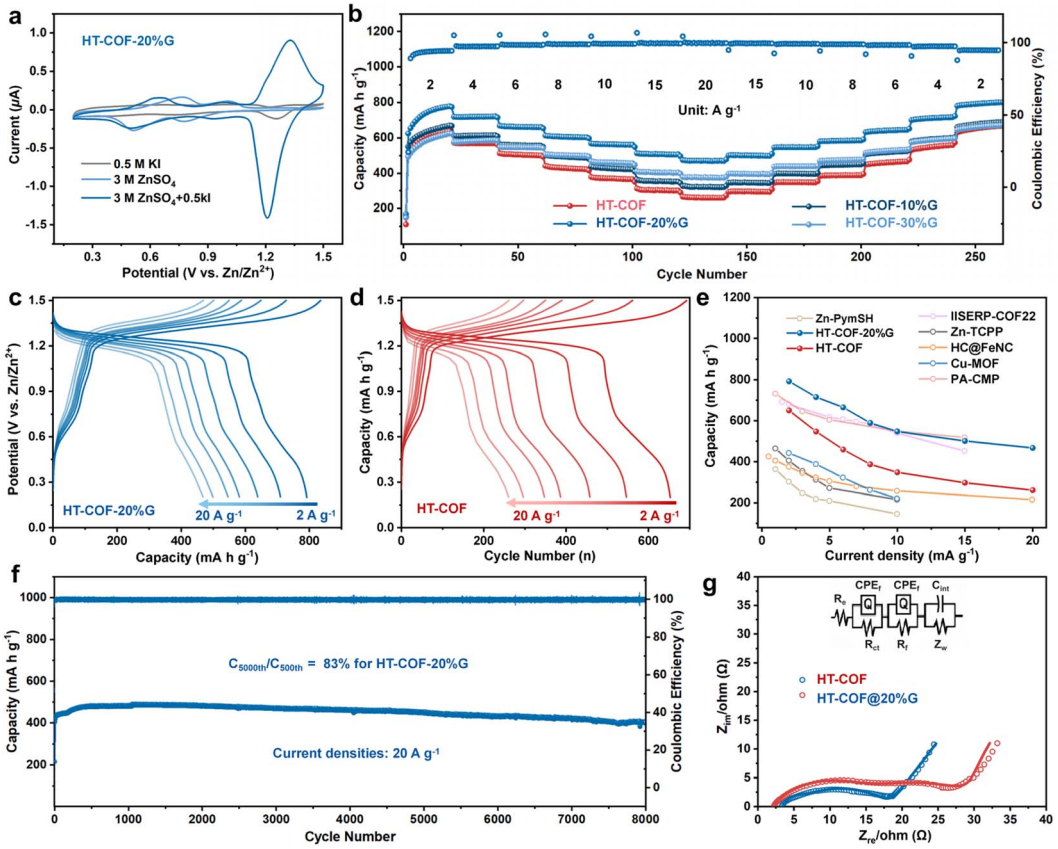

Fig. 3 Electrochemical performance of HT-COF and HT-COF-XG. (a) Comparative CV plots of the HT-COF-20%G-based coin cells measured using different electrolytes at 0.2 mV s^{-1} (for convenience of comparison, the CV curve is normalized by weight of active substance). (b) Rate performance of HT-COF-20%G and HT-COF electrodes from 2 to 10 A g^{-1}. (c and d) GCD curves of the HT-COF-20%G and HT-COF electrodes at different current densities corresponding to the rate performance in the 130th, 150th, 170th, 190th, 210th, 230th and 250th cycles. (e) Rate performance comparison between HT-COF-20%G and other organic framework materials. (f) Cycling performance of the HT-COF-20%G electrode. (g) Nyquist plots of the HT-COF-20%G and HT-COF electrodes.

performance compared to HT-COF-10%G and HT-COF under high current densities, particularly at 20 A g^{-1}, due to the optimized ion transport pathways and enhanced electrical conductivity of HT-COF-30%G. The HT-COF-20%G electrode exhibits the best rate performance of the HT-COF-XG cathodes and demonstrates an optimal balance between the active site utilization efficiency, the number of exposed sites, and conductivity. The electrochemical performance of HT-COF-20% G is also superior to that of HT-COF@20%G (a physical mixture of graphene and HT-COFs, Fig. S19), proving the high utilization of the active sites of the HT-COF-20%G nanosheets. In particular, the HT-COF-20%G cathode exhibits the best rate performance for rechargeable ADIBs reported to date (Fig. 3e and Table S1). On the basis of the discharge capacity and average discharge voltage, the energy density of the HT-COF-20%G electrode amounts to 870 W h kg^{-1}, representing the best performance for an ADIBs cathode. Remarkably, the HT-COF-20%G cathode can deliver an exceptional energy density of 461 W h kg^{-1} even under a high current density of 20 A g^{-1}, corresponding to a power density of 22 734 W kg^{-1} with a complete discharge time of 73 seconds. These results reveal the great advantages that the COF/graphene nanosheets have for use in ADIBs.

The long-term cycling performance of HT-COF-20%G was further assessed at a high current density of 20 A g^{-1}. As exhibited in Fig. 3f, the capacity of the HT-COF-20%G electrode remains stable at 404 mAh g^{-1} even after 8000 cycles with an excellent capacity retention rate of 83%, representing one of the best COF-based ADIBs electrodes in terms of both long cycling stability and high capacity (Table S1). To probe the reason for the capacity decay, which is particularly pronounced after 5000 cycles, the cycled HT-COF-20%G cell was disassembled for post-mortem analysis. As shown in Fig. S20a, the yellow stains observed on the separator unambiguously indicate the occurrence of the dissolution and shuttling effect during the charge–discharge process.[48,49] SEM images of the cycled zinc anode display substantial dendrite formation and surface passivation (Fig. S20b and c), confirming the occurrence of uneven zinc deposition during the charge–discharge process.[50,51] Additionally, the TEM image of the cycled HT-COF-20%G cathode manifests a lowered degree of structural order (Fig. S21) suggesting gradual degradation of the active material after prolonged cycling. These observations reveal that the capacity

fading primarily originates from three factors: polyiodide dissolution/shuttling, zinc dendrite formation, and the structural degradation of the active HT-COF-20%G material. To quantitatively evaluate the contribution of each factor, a new coin cell was reassembled using the cycled HT-COF-20%G cathode with a fresh electrolyte and zinc anode. After initial activation, the reassembled cell delivers a stable capacity of around 437 mAh g^{-1} at 20 A g^{-1}, Fig. S22, corresponding to 91% of its original capacity. This result indicates that 9% of the capacity loss for the initial HT-COF-20%G cell after 8000 cycles is attributed to the degradation of the HT-COF-20%G cathode, while the remaining 8% of the capacity loss is caused by polyiodide shuttling and zinc anode degradation.

To further assess the charge–discharge stability in depth, the cycling behavior was also examined at a lower current density. The gradual increase in capacity during the initial cycles is attributed to a progressive electrode activation process, which improves electrolyte wetting and enhances the accessibility of the porous framework to ions. As shown in Fig. S23, the HT-COF-20%G electrode maintains a stable capacity of 760 mAh g^{-1} at 2 A g^{-1} over 500 cycles, demonstrating the good cycling stability of HT-COF-20%G electrode under both high and low current densities. Electrochemical impedance spectroscopy (EIS) analysis reveals that HT-COF-20%G exhibits a significantly reduced resistance of 18.3 Ω in comparison with HT-COF (26.5 Ω) (Fig. 3g), indicating enhanced charge transfer kinetics for this COF/graphene-based electrode. This point is further supported by the smaller charge transfer impedance (R_{ct}) of HT-COF-20%G (6.6 Ω) compared to that of HT-COF (12.1 Ω) in coin cells. Subsequently, the Warburg coefficient of the HT-COF-20% G-based cell is calculated to be 1.04 Ω $s^{1/2}$, lower than that of HT-COF (1.39 Ω$s^{1/2}$, Fig. S24), suggesting that the faster ion diffusion kinetics of HT-COF-20%G are due to the shortened pathway for ion diffusion and the enhanced accessibility of the active sites in the COF nanosheets. These results demonstrate the enhanced ion and electron conductivity of the COF/graphene nanosheets, which are beneficial for improving the battery performance. To further reveal the evolution of the internal resistance in the HT-COF-20%G electrode after cycling, EIS measurements after 8000 cycles were recorded. The resistance of the HT-COF-20%G battery is 12.6 Ω (Fig. S25) which is lower than the total impedance of the fresh coin cell. This result suggests that long-term cycling enhances electrolyte wettability and optimizes the contact at the solid–liquid interface, ultimately resulting in a reduction in the impedance.

Electrochemical mechanism

To gain insights into the mechanism underlying the enhanced rate performance, the electrical conductivities of HT-COF, HT-COF-XG and HT-COF@XG were comparatively investigated. As illustrated in Fig. 4a and S26, the electrical conductivity of HT-COF was determined to be 1.56 × 10^{-5} S m^{-1}, whereas the electrical conductivity of HT-COF-20%G is increased to 1.16 × 10^{-1} S m^{-1}. This significant enhancement unveils the largely improved conductive properties of the COF/graphene composites. Furthermore, at identical graphene loadings (10, 20, and 30 wt%), the conductivity of *in situ* grown HT-COF-XG samples (2.03 × 10^{-3} S m^{-1} for HT-COF-10%G, 1.16 × 10^{-1} S m^{-1} for HT-COF-20%G, and 14.8 S m^{-1} for HT-COF-30%G) is 1–2 orders of magnitude higher compared to their physically mixed counterparts (7.41× 10^{-5} S m^{-1} for HT-COF@10%G, 3.07 × 10^{-4} S m^{-1} for HT-COF@20%G, and 1.88 × 10^{-3} S m^{-1} for HT-COF@30%G). This result implies that the superior interfacial contact quality achieved through the *in situ* growth strategy is able to promote efficient charge transfer across the COF/graphene interface, contributing to the enhanced conductivity of HT-COF-XG. To further understand the ion transport kinetics, a series of CV curves were recorded at scan rates of 0.4, 0.6, 1.0, 2.0, and 5.0 mV s^{-1}. The CV curves exhibit a consistent shape across different scan rates, with the peak area gradually increasing as the sweep speed increases (Fig. 4b). Notably, the peak currents do not show a proportional relationship with the square root of the scan rates, indicating the occurrence of both faradaic and non-faradaic reactions during the ion storage process. Generally, the relationship between the measured peak current (i) and sweep rate (v) in CV curves can be mathematically described by a power law equation, $\log(i) = \log(a) + b \times \log(v)$, where a and b represent adjustable parameters. The calculated b values for the oxidation peaks of O_1, O_2, and O_3 are 0.87, 0.89, and 0.83, respectively, while the b values for R_1, R_2, and R_3 are 0.78, 0.92, and 0.58 (Fig. 4c). These results suggest that charge storage occurs through a rapid capacitive-dominated process facilitated by unhindered ion diffusion within the ordered channels of the COF/graphene nanosheets and through the enhanced reactivity of accessible active sites in HT-COF-20%G.[52] Additionally, the diffusion-controlled and capacitive contributions in the HT-COF-20%G battery system can be quantitatively separated using Trasatti analysis.[53] As illustrated in Fig. 4d, e and S27, the capacitive contribution is determined to be 55.6% at a scan rate of 0.4 mV s^{-1}, which further increases to 80.3% at 5 mV s^{-1}. These results suggest a rapid kinetic capacitive process in ion storage for the HT-COF-20%G cathode, attributed to both facile charge carrier transport within the exposed active sites on the nanosheets and excellent conductivity.

To investigate the ion insertion mechanism of the HT-COF-XG nanosheets, *ex situ* FT-IR analysis on a representative HT-COF-20%G electrode at different stages was carried out (Fig. 4f–i). As displayed in Fig. 4f, the characteristic peaks at 1778, 1724, and 738 cm^{-1} corresponding to the asymmetric stretching, symmetric stretching, and in-plane shear vibration of the C=O of the imide moieties could be observed for the fresh electrode. These signals gradually weakened during the discharge process. Meanwhile, the conjugated C=N component bands of the HATN moieties at 1510–1583 and 1183 cm^{-1} are also weakened in a gradual manner along with a gradual increase in the intensity of the C–N vibration band at 1636 cm^{-1} accompanied by a blue shift of the C–N vibration bands at 1350 and 1077 cm^{-1} during the discharge process.[54] After being fully recharged to 1.2 V, the band intensity of these groups returns to the original state, demonstrating their reversibility evolution during the discharge/charge process. Subsequently, upon further charging to 1.5 V, two new peaks at 1043 and 875 cm^{-1}

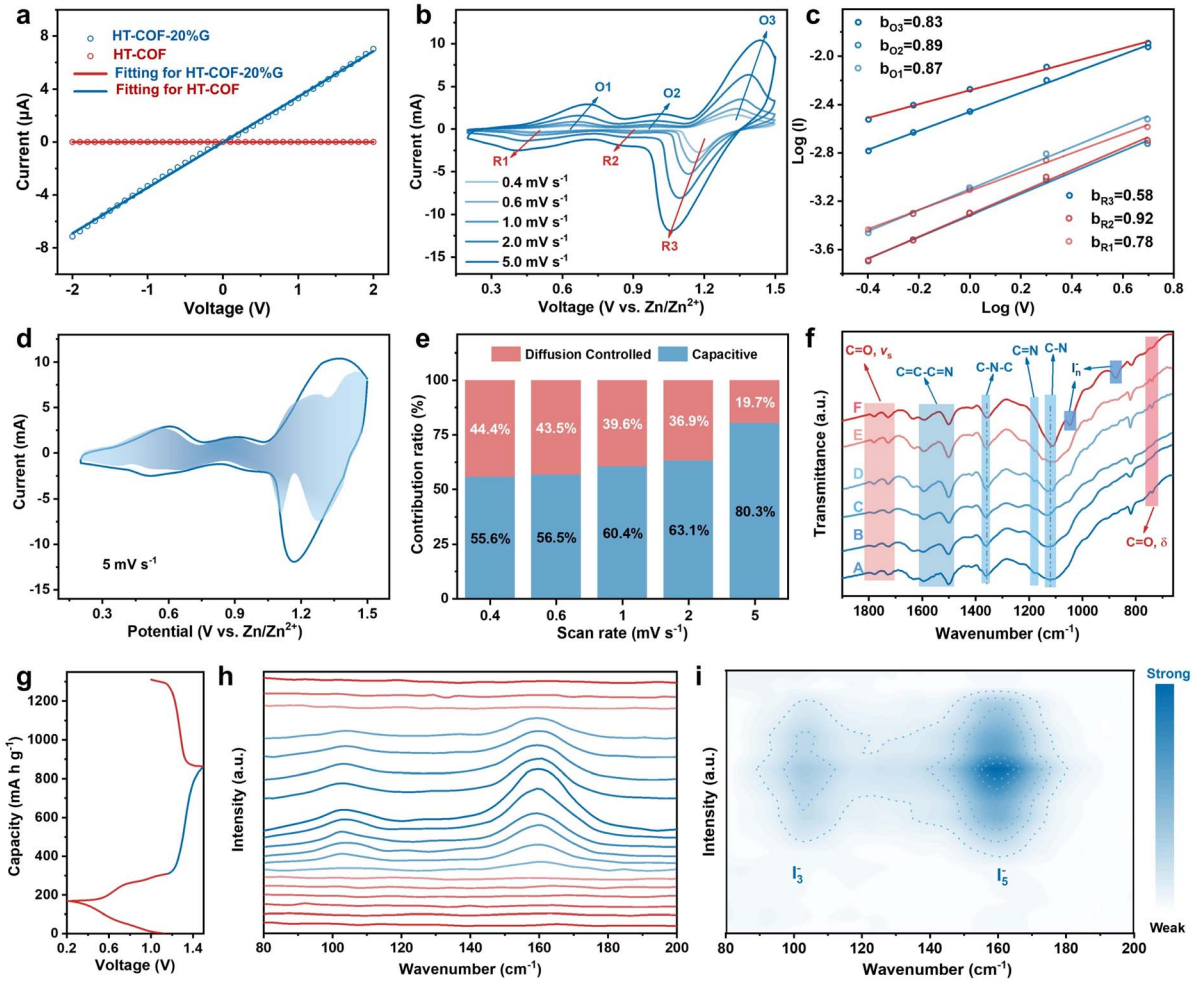

Fig. 4 Electrochemical mechanism of HT-COF-20%G. (a) Current–voltage curves of HT-COF-20%G and HT-COF at 298 K. (b) CV profiles of the HT-COF-20%G electrode at various scan rates. O_n and R_n ($n = 1$–3) represent the oxidation and reduction peaks, respectively. (c) Determination of the *b* values of the oxidation and reduction peaks. (d) Capacitive-controlled contribution at 5.0 mV s^{-1}. (e) Contribution ratios controlled by the capacitance at different scan rates. (f) *Ex situ* FT-IR spectra of different states (A: fresh electrode; B: discharged to 0.5 V; C: discharged to 0.2 V; D: charged to 0.9 V; E: charged to 1.2 V; F: charged to 1.5 V). (g–i) *In situ* Raman analysis of the HT-COF-20%G electrodes during cycling.

attributed to the iodine species emerged accompanied by a reduced peak intensity of the C=O and C=N components. These findings indicate an enrichment of the iodine species in the HT-COF-20%G electrode material and their interaction with the functional groups of HT-COF. Furthermore, *ex situ* X-ray photoelectron spectroscopy (XPS) was conducted to further clarify the reversible transformation of these functional active components in different states (Fig. S28a and b). As can be seen, the N 1s XPS spectrum of the HT-COF-20%G electrode can be fitted into two peaks assigned to the C=N groups in HATN (399.5 eV) and the triazine moieties and the C–N groups (400.4 eV) in the imide moieties.[55] Meanwhile, only the peak assigned to the X = O (X = C and O) bonds at 532.6 eV is observed in the O 1s XPS spectrum.[56] After discharging to 0.2 V, the intensity of both the C=N and X = O groups is significantly diminished, while the intensity of the C–N and C–O bonds is increased. Moreover, the relative intensity is recovered after charging to 1.5 V *versus* Zn/Zn^{2+}. Simultaneously, new peaks are observed at 389.9 and 531.7 eV in the N 1s and O 1s XPS spectra, respectively, which are attributed to the interactions of C=N/C=O with I_n^-.[28] These peaks are further enhanced after charging to 1.5 V, indicating the storage of I_n^- as an electron acceptor through interaction with its vacant σ* antibonding orbital by the lone pair electrons of the C=N and C=O groups. In the I 3d XPS spectrum (Fig. S28c) a transformation from I^- to I_n^- can be observed that is consistent with the IR spectroscopic results (Fig. 4f). These results demonstrate that HT-COF-20%G not only undergoes redox reactions to store charge carriers but also adsorbs active I_n^- ions in the electrolyte, thereby significantly enhancing the specific capacity of the electrode. Nevertheless, *in situ* Raman spectroscopic measurements provide further insight into the transformation of the iodine species induced by the HT-COF-20%G cathodes (Fig. 4g–i). When charging to 1.15 V, two new peaks appeared at 110 and 160 cm^{-1} attributed to I_3^- and I_5^-, respectively, suggesting that I^- was oxidized into I_3^-/I_5^-.[57] Specifically, I^- is initially oxidized to I_2. Subsequently, the reaction between I^- and I_2 occurs as follows: $I^- + I_2 \rightleftharpoons I_3^-$, and further proceeds to $I_3^- + I_2 \rightleftharpoons I_5^-$. The

intensities of the peaks for these new species increase in a continuous manner until reaching a maximum at the end of the charging process. In the following discharge process, these two peaks disappear, proving the reversible nature of the transition between I^- and I_3^-/I_5^-.

DFT calculations

In order to clarify the nature of the Zn^{2+}/I_n^- ($n = 3, 5$) adsorbing/desorbing pathways and the electrode-driven I_n^-/I^- conversion mechanism, particularly the unique advantages of combing HT-COF with a graphene substrate to enhance conductivity, a density-functional theory (DFT) study was carried out at the M06-2X-D3/SDD (for I)/6-311G(d) (for other atoms) level of theory.[58–61] Detailed calculation settings are listed in the SI.

Firstly, to understand the interaction between HT-COF and graphene in the composite nanosheets, the charge density difference of HT-COF-20%G was calculated. As shown in Fig. S29, the electron cloud transfers from graphene to HT-COF, leading to a tight π–π interaction between the graphene and HT-COF. More importantly, the π–LOL calculation result explains the uniform conjugated conductive structure of HT-COF (Fig. 5a) which facilitates the smooth transfer of electrons along the current collector ↔ graphene ↔ HT-COF ↔ solvent route.

Using this smooth electron transfer route, the full charging/discharging mechanism on the HT-COF-20%G electrode could be divided into four stages: (1) Zn^{2+} storage is the first discharge process; (2) Zn^{2+} release is the first charging process; (3) $I^- \rightarrow I_n^-$ conversion is the continuous charging process; and (4) $I_n^- \rightarrow I^-$ conversion is the last discharge process. The full charge/discharge cycle is described in the following equations:

Stage 1, first discharge process, $\Delta_r G_{m_1}^{\theta} = 1.99$ eV:

$$[O_2N_2] + 4e^- + 2Zn^{2+} \rightarrow [O_2N_2]^{4-}\cdot 2Zn^{2+} \quad (1)$$

Stage 2, first charging process, $\Delta_r G_{m_2}^{\theta} = -1.99$ eV:

$$[O_2N_2]^{4-}\cdot 2Zn^{2+} - 4e^- \rightarrow [O_2N_2] + 2Zn^{2+} \quad (2)$$

Stage 3, continuous charging, $\Delta_r G_{m_3}^{\theta} = 1.46$ eV ($n = 3$) or 1.85 eV ($n = 5$):

$$[O_2N_2] + (2n)I^- - 2(n-1)e^- + 2K^+ \rightarrow [O_2N_2]\cdot 2I_n^-\cdot 2K^+ \quad (3)$$

Stage 4, last discharge process, $\Delta_r G_{m_4}^{\theta} = -1.46$ eV ($n = 3$) or -1.85 eV ($n = 5$):

$$[O_2N_2]\cdot 2I_n^-\cdot 2K^+ + 2(n-1)e^- \rightarrow [O_2N_2] + (2n)I^- + 2K^+ \quad (4)$$

Before discussing the reaction mechanism, we must first recheck the structure of HT-COF. As can be seen in Fig. 1d and S30, each six-membered hole of HT-COF contains three ion adsorption sites (named as the three $[O_2N_2]$ sites) constructed from six C=O groups and six C=N groups that are arranged together in a densely packed but orderly fashion. Electrostatic potential (EP) calculations show that each six-membered hole, which contains three $[O_2N_2]^{4-}$ sites, could chelate six Zn^{2+} ions per hole (Fig. 5b). As the starting point of the first stage, four electrons ($4e^-$) would be injected into the HT-COF-20%G electrode changing two C=O and two C=N groups into two $C–O^-$ and two $C–N^-$ groups in each $[O_2N_2]$ site. At the same time, two dissociated Zn^{2+} ions in the solvent would be immediately attracted by each $[O_2N_2]^{4-}$ site (eqn (1) and Fig. 5c) in line with the XPS and FT-IR analysis results. In the first discharge stage,

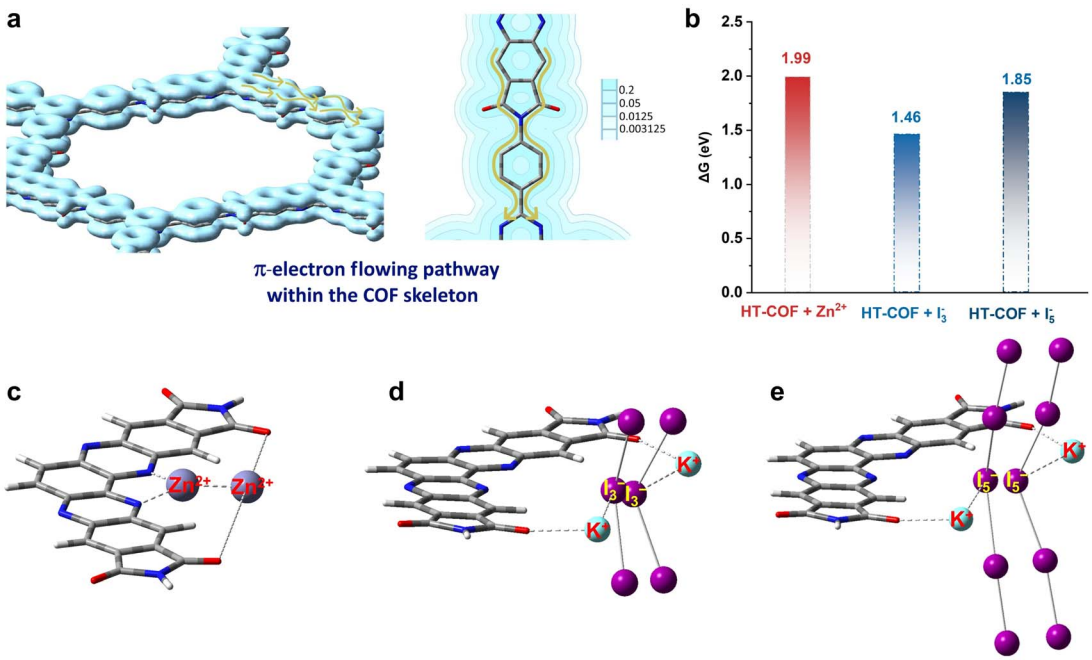

Fig. 5 DFT calculations for the HT-COF storage of Zn^{2+} and the polyiodides. (a) The π-electron flowing pathway within the HT-COF skeleton. (b) The electrostatic potential map of HT-COF. (c–e) The simulated adsorption of the Zn^{2+} ions, I_3^- ions and I_5^- ions by the $[O_2N_2]$ sites.

the storage of Zn^{2+}, HT-COF shows two advantages: (1) HT-COF possesses densely packed but orderly arranged redox sites which can capture the abundant Zn^{2+} ions in the manner of chelate compound $[O_2N_2]^{4-}\cdot 2Zn^{2+}$; and (2) HT-COF-20%G performs excellently in the electron transfer route due to the tight interaction and charge transfer between the graphene and HT-COF together with the uniform conjugated conductive structure of HT-COF.

As a reverse process of Stage 1, $4e^-$ and $2Zn^{2+}$ ions would be released out of the HT-COF-20%G electrode in Stage 2, in which $[O_2N_2]^{4-}\cdot 2Zn^{2+}$ is oxidized back to $[O_2N_2]$ (eqn (2)). However, the charging process would certainly not stop at Stage 2. After the chelated Zn^{2+} ions are exhausted, the continuous charging process, Stage 3, will be started, in which an extra $2(n-1)$ electrons ($n = 3, 5$) would be continuously released through the conversion of I_n^-/I^-, providing extra battery capacity to the present ADIB. Theoretical calculations indicate that the advantage of HT-COF in Stage 3 is that the $[O_2N_2]$ group can effectively anchor the I_3^- and I_5^- ions with a strong adsorption energy of 1.46 and 1.85 eV, respectively (Fig. 5d and e). Finally, the extra $2(n-1)$ electrons released in the charging stage should be returned to the electrode HT-COF-20%G in Stage 4, completing the full charge/discharge cycle. In short, due to the introduction of HT-COF/I_n^-, the battery possesses an extra $2(n-1)$ electrons in the charge/discharge process.

When we look back to the full reaction mechanism, two advantages of HT-COF can be summarized: (1) HT-COF possesses densely packed but orderly arranged redox $[O_2N_2]$ sites which can be used by the Zn^{2+} and I_n^- ions at different stages. This is responsible for the high capacity of the battery. (2) As the key component of HT-COF-20%G, HT-COF facilitates smooth electron transfer along the current collector ↔ graphene ↔ HT-COF ↔ solvent route. This is responsible for the high conductivity of the battery.

Last but not least, the ionic sizes of solvated $[Zn(H_2O)_6]^{2+}$, $[K(H_2O)_6]^+$, I_3^-, and I_5^- were calculated using DFT. As shown in Fig. S31, the solvated ionic sizes are calculated to be approximately 0.61 nm for $[Zn(H_2O)_6]^{2+}$, 0.78 nm for $[K(H_2O)_6]^+$, 0.99 nm (long axis diameter) multiplied by 0.45 nm (short axis diameter) for I_3^-, and 1.44 nm (long axis diameter) multiplied by 0.46 nm (short axis diameter) for I_5^-, significantly smaller than the pore size of HT-COF, thus favoring efficient ion transport and storage and in turn leading to the excellent rate performance of the ADIBs.

Conclusions

In summary, the use of building blocks with an aromatic conjugated structure induces the formation of thin COF nanosheets on graphene that maintain their crystallinity. This structure imparts the graphene-supported thin 2D COF nanosheets with enhanced conductivity, more exposed active sites, and a shortened ion transport path. The combination of these factors endows HT-COF-20%G with the best ADIB performance to date. As exemplified by its remarkable energy and power densities. The present result offers valuable insight into the development of substrate-supported COF nanosheets with exceptional electrochemical properties, further unlocking their potential in sustainable energy storage applications.

Author contributions

J. Jiang, K. Wang, Q. Chen, and X. Yang conceived and supervised the project, X. Yang and M. Huang performed the synthesis experiments, X. Yang, G. Lu, R. Jiang, and X. Wang performed the experimental characterization, X. Yang, M. Huang, and Z. Liu performed the battery tests, D. Qi performed the DFT calculations, J. Jiang, K. Wang, Q. Chen, X. Yang, L. Jiao, and E. Hao linked the experiments, analysis and calculations, and all the authors discussed and wrote the manuscript.

Conflicts of interest

There are no conflicts to declare.

Data availability

The data supporting the findings of this study are available within the article or supplementary information (SI). Supplementary information: experimental details, thermogravimetric (TG) curves, physical and PXRD images, charge–discharge curves, and calculation details. See DOI: **https://doi.org/10.1039/d5sc04918k**.

Acknowledgements

We gratefully acknowledge the financial support from the Natural Science Foundation of China (No. 22235001 and 22175020) and Launch Fund of Anhui Normal University (2025GFXK005).

Notes and references

1 B. Lee, Y. Ko, G. Kwon, S. Lee, K. Ku, J. Kim and K. Kang, *Joule*, 2018, **2**, 61–75.
2 L. Geng, J. Meng, X. Wang, W. Wu, K. Han, M. Huang, C. Han, L. Wu, J. Li, L. Zhou and L. Mai, *Chem*, 2025, **11**, 102302.
3 C. Zhong, B. Liu, J. Ding, X. Liu, Y. Zhong, Y. Li, C. Sun, X. Han, Y. Deng, N. Zhao and W. Hu, *Nat. Energy*, 2020, **5**, 440–449.
4 Z. Huang, X. Li, Z. Chen, P. Li, X. Ji and C. Zhi, *Nat. Rev. Chem.*, 2023, **7**, 616–631.
5 Z. Huang, Y. Hou, T. Wang, Y. Zhao, G. Liang, X. Li, Y. Guo, Q. Yang, Z. Chen, Q. Li, L. Ma, J. Fan and C. Zhi, *Nat. Commun.*, 2021, **12**, 3106.
6 C. Zhang, W. Ma, C. Han, L.-W. Luo, A. Daniyar, S. Xiang, X. Wu, X. Ji and J.-X. Jiang, *Energy Environ. Sci.*, 2021, **14**, 462–472.
7 Z. Zhao and H. N. Alshareef, *Adv. Mater.*, 2024, **36**, 2309223.
8 K. Zhou, G. Liu, X. Zhu, G. Liu, X. Yu, Z. Guo and Y. Wang, *Angew. Chem., Int. Ed.*, 2025, **64**, e202413959.

9 K. Shin, Y. Pei, X. Zhou, Q. Chen, P. Kidkhunthod, Y. Zheng, X. Guo, S. Tunmee, Q. Zhang and Y. Tang, *Adv. Mater.*, 2025, **37**, 2413645.
10 D. Chao, C. Ye, F. Xie, W. Zhou, Q. Zhang, Q. Gu, K. Davey, L. Gu and S.-Z. Qiao, *Adv. Mater.*, 2020, **32**, 2001894.
11 C. Guo, B. Han, W. Sun, Y. Cao, Y. Zhang and Y. Wang, *Angew. Chem., Int. Ed.*, 2022, **61**, e202213276.
12 K. Zhang, Q. Yu, J. Sun, Z. Tie and Z. Jin, *Adv. Mater.*, 2024, **36**, 2309838.
13 G. Wang, M. Zhu, G. Chen, Z. Qu, B. Kohn, U. Scheler, X. Chu, Y. Fu, O. G. Schmidt and X. Feng, *Adv. Mater.*, 2022, **34**, 2201957.
14 H. Zhang, L. Zhong, J. Xie, F. Yang, X. Liu and X. Lu, *Adv. Mater.*, 2021, **33**, 2101857.
15 M. Liu, Q. Chen, X. Cao, D. Tan, J. Ma and J. Zhang, *J. Am. Chem. Soc.*, 2022, **144**, 21683–21691.
16 H. Yang, Y. Qiao, Z. Chang, H. Deng, P. He and H. Zhou, *Adv. Mater.*, 2020, **32**, 2004240.
17 T. Xiao, J.-L. Yang, B. Zhang, J. Wu, J. Li, W. Mai and H. J. Fan, *Angew. Chem., Int. Ed.*, 2024, **63**, e202318470.
18 J. Hao, L. Yuan, Y. Zhu, X. Bai, C. Ye, Y. Jiao and S.-Z. Qiao, *Angew. Chem., Int. Ed.*, 2023, **62**, e202310284.
19 J.-L. Yang, T. Xiao, T. Xiao, J. Li, Z. Yu, K. Liu, P. Yang and H. J. Fan, *Adv. Mater.*, 2024, **36**, 2313610.
20 Y. Tan, Z. Chen, Z. Tao, A. Wang, S. Lai and Y. Yang, *Angew. Chem., Int. Ed.*, 2023, **62**, e202217744.
21 Y. Tan, Z. Tao, Y. Zhu, Z. Chen, A. Wang, S. Lai and Y. Yang, *ACS Appl. Mater. Interfaces*, 2022, **14**, 47716–47724.
22 P. Bao, L. Cheng, X. Yan, X. Nie, X. Su, H.-G. Wang and L. Chen, *Angew. Chem., Int. Ed.*, 2024, **63**, e202405168.
23 Y. Hu, B. Sengupta, H. Long, L. J. Wayment, R. Ciora, Y. Jin, J. Wu, Z. Lei, K. Friedman, H. Chen, M. Yu and W. Zhang, *Science*, 2024, **384**, 1441–1447.
24 S. S. Han, H. Furukawa, O. M. Yaghi and W. A. Goddard, III, *J. Am. Chem. Soc.*, 2008, **130**, 11580–11581.
25 X. Yang, L. Gong, K. Wang, S. Ma, W. Liu, B. Li, N. Li, H. Pan, X. Chen, H. Wang, J. Liu and J. Jiang, *Adv. Mater.*, 2022, **34**, 2207245.
26 S. E. Neumann, J. Kwon, C. Gropp, L. Ma, R. Giovine, T. Ma, N. Hanikel, K. Wang, T. Chen, S. Jagani, R. O. Ritchie, T. Xu and O. M. Yaghi, The propensity for covalent organic frameworks to template polymer entanglement, *Science*, 2024, **383**, 1337–1343.
27 Z. Liu, W. Liu, Y. Chen, X. Yang, Y. Liu, Y. Jin, Q. Xu, D. Qi, K. Wang, Y. Zhu and J. Jiang, *CCS Chem.*, 2025, **7**, 1812–1822.
28 R. Kushwaha, C. Jain, P. Shekhar, D. Rase, R. Illathvalappil, D. Mekan, A. Camellus, C. P. Vinod and R. Vaidhyanathan, *Adv. Energy Mater.*, 2023, **13**, 2301049.
29 J. Li, X. Jing, Q. Li, S. Li, X. Gao, X. Feng and B. Wang, *Chem. Soc. Rev.*, 2020, **49**, 3565–3604.
30 S. Wang, Q. Wang, P. Shao, Y. Han, X. Gao, L. Ma, S. Yuan, X. Ma, J. Zhou, X. Feng and B. Wang, *J. Am. Chem. Soc.*, 2017, **139**, 4258–4261.
31 K. Koner, H. S. Sasmal, D. Shetty and R. Banerjee, *Angew. Chem., Int. Ed.*, 2024, **63**, e202406418.
32 H. Duan, K. Li, M. Xie, J.-M. Chen, H.-G. Zhou, X. Wu, G.-H. Ning, A. I. Cooper and D. Li, *J. Am. Chem. Soc.*, 2021, **143**, 19446–19453.
33 S. Gu, S. Wu, L. Cao, M. Li, N. Qin, J. Zhu, Z. Wang, Y. Li, Z. Li, J. Chen and Z. Lu, *J. Am. Chem. Soc.*, 2019, **141**, 9623–9628.
34 B. Wang, L. Shen, Y. He, C. Chen, Z. Yang, L. Fei, J. Xu, B. Li and H. Lin, *Small*, 2024, **20**, 2310174.
35 H. Gao, Q. Zhu, A. R. Neale, M. Bahri, X. Wang, H. Yang, L. Liu, R. Clowes, N. D. Browning, R. S. Sprick, M. A. Little, L. J. Hardwick and A. I. Cooper, *Adv. Energy Mater.*, 2021, **11**, 2101880.
36 X.-X. Luo, W.-H. Li, H.-J. Liang, H.-X. Zhang, K.-D. Du, X.-T. Wang, X.-F. Liu, J.-P. Zhang and X.-L. Wu, *Angew. Chem., Int. Ed.*, 2022, **61**, e202117661.
37 X. Liu, Y. Jin, H. Wang, X. Yang, P. Zhang, K. Wang and J. Jiang, *Adv. Mater.*, 2022, **34**, 2203605.
38 H. Gao, A. R. Neale, Q. Zhu, M. Bahri, X. Wang, H. Yang, Y. Xu, R. Clowes, N. D. Browning, M. A. Little, L. J. Hardwick and A. I. Cooper, *J. Am. Chem. Soc.*, 2022, **144**, 9434–9442.
39 Q. Xu, Z. Liu, Y. Jin, X. Yang, T. Sun, T. Zheng, N. Li, Y. Wang, T. Li, K. Wang and J. Jiang, *Energy Environ. Sci.*, 2024, **17**, 5451–5460.
40 T. Kim, S. H. Joo, J. Gong, S. Choi, J. H. Min, Y. Kim, G. Lee, E. Lee, S. Park, S. K. Kwak, H.-S. Lee and B.-S. Kim, *Angew. Chem., Int. Ed.*, 2022, **61**, e202113780.
41 X. Yang, L. Gong, Y. Jin, T. Zheng, X. Wang, Q. Zhi, B. Yu, K. Wang and J. Jiang, *CCS Chem.*, 2025, **7**, 3063–3075.
42 Y. Jiang, Z. Zhang, D. Chen, J. Du, Y. Yang, S. Wang, F. Guo, X. Chen, C. Gao, W.-J. Wang and P. Liu, *Adv. Mater.*, 2022, **34**, 2204250.
43 C. Li, P. Guggenberger, S. W. Han, W.-L. Ding and F. Kleitz, *Angew. Chem., Int. Ed.*, 2022, **61**, e202206564.
44 Y. Bai, Y. Liu, M. Liu, X. Wang, S. Shang, W. Gao, C. Du, Y. Qiao, J. Chen, J. Dong and Y. Liu, *Angew. Chem., Int. Ed.*, 2022, **61**, e202113067.
45 J. Sun, A. Klechikov, C. Moise, M. Prodana, M. Enachescu and A. V. Talyzin, *Angew. Chem., Int. Ed.*, 2018, **57**, 1034–1038.
46 W. Wang, V. S. Kale, Z. Cao, Y. Lei, S. Kandambeth, G. Zou, Y. Zhu, E. Abouhamad, O. Shekhah, L. Cavallo, M. Eddaoudi and H. N. Alshareef, *Adv. Mater.*, 2021, **33**, 2103617.
47 Y. Chen, J. Li, Q. Zhu, K. Fan, Y. Cao, G. Zhang, C. Zhang, Y. Gao, J. Zou, T. Zhai and C. Wang, *Angew. Chem., Int. Ed.*, 2022, **61**, e202116289.
48 V. Yadav, M. A. Siegler and D. P. Goldberg, *J. Am. Chem. Soc.*, 2021, **143**, 46–52.
49 S. Haldar, M. Wang, P. Bhauriyal, A. Hazra, A. H. Khan, V. Bon, M. A. Isaacs, A. De, L. Shupletsov, T. Boenke, J. Grothe, T. Heine, E. Brunner, X. Feng, R. Dong, A. Schneemann and S. Kaskel, *J. Am. Chem. Soc.*, 2022, **144**, 9101–9112.
50 Q. Yang, Q. Li, Z. Liu, D. Wang, Y. Guo, X. Li, Y. Tang, H. Li, B. Dong and C. Zhi, *Adv. Mater.*, 2020, **32**, 2001854.
51 F. Bu, Z. Sun, W. Zhou, Y. Zhang, Y. Chen, B. Ma, X. Liu, P. Liang, C. Zhong, R. Zhao, H. Li, L. Wang, T. Zhang,

B. Wang, Z. Zhao, J. Zhang, W. Li, Y. S. Ibrahim, Y. Hassan, A. Elzatahry, D. Chao and D. Zhao, *J. Am. Chem. Soc.*, 2023, **145**, 24284–24293.

52 G. Wang, N. Chandrasekhar, B. P. Biswal, D. Becker, S. Paasch, E. Brunner, M. Addicoat, M. Yu, R. Berger and X. Feng, *Adv. Mater.*, 2019, **31**, 1901478.

53 S. Ardizzone, G. Fregonara and S. Trasatti, *Electrochim. Acta*, 1990, **35**, 263–267.

54 Z. Tian, V. S. Kale, Y. Wang, S. Kandambeth, J. Czaban-Jóźwiak, O. Shekhah, M. Eddaoudi and H. N. Alshareef, *J. Am. Chem. Soc.*, 2021, **143**, 19178–19186.

55 Z. Tie, L. Liu, S. Deng, D. Zhao and Z. Niu, *Angew. Chem., Int. Ed.*, 2020, **59**, 4920–4924.

56 X. Yang, L. Gong, X. Liu, P. Zhang, B. Li, D. Qi, K. Wang, F. He and J. Jiang, *Angew. Chem., Int. Ed.*, 2022, **61**, e202207043.

57 Y. Wang, X. Jin, J. Xiong, Q. Zhu, Q. Li, R. Wang, J. Li, Y. Fan, Y. Zhao and X. Sun, *Adv. Mater.*, 2024, **36**, 2404093.

58 Y.-S. Lin, G.-D. Li, S.-P. Mao and J.-D. Chai, *J. Chem. Theory Comput.*, 2013, **9**, 263–272.

59 A. D. McLean and G. S. Chandler, *J. Chem. Phys.*, 1980, **72**, 5639–5648.

60 R. Krishnan, J. S. Binkley, R. Seeger and J. A. Pople, *J. Chem. Phys.*, 1980, **72**, 650–654.

61 M. M. Francl, W. J. Pietro, W. J. Hehre, J. S. Binkley, M. S. Gordon, D. J. DeFrees and J. A. Pople, *J. Chem. Phys.*, 1982, **77**, 3654–3665.